Mapping remodeling of thalamocortical projections in the living *reeler* mouse brain by diffusion tractography

Laura-Adela Harsan[a,1,2], Csaba Dávid[b,1], Marco Reisert[a], Susanne Schnell[a,c], Jürgen Hennig[a], Dominik von Elverfeldt[a], and Jochen F. Staiger[d,e]

[a]Department of Radiology, Medical Physics, University Medical Center and the BrainLinks-BrainTools Excellence Cluster of the University of Freiburg, 79106 - Freiburg, Germany; [b]Department of Human Morphology and Developmental Biology, Semmelweis University, Budapest, H-1094, Hungary; [c]Department of Radiology, Feinberg School of Medicine, Northwestern University, Chicago, IL 60611-2927; and [d]Department of Neuroanatomy and [e]Deutsche Forschungsgemeinschaft Center for Molecular Physiology of the Brain/Excellence Cluster 171, Georg-August University, 37075 Göttingen, Germany

Edited by Marcus E. Raichle, Washington University in St. Louis, St. Louis, MO, and approved March 29, 2013 (received for review October 23, 2012)

A major challenge in neuroscience is to accurately decipher in vivo the entire brain circuitry (connectome) at a microscopic level. Currently, the only methodology providing a global noninvasive window into structural brain connectivity is diffusion tractography. The extent to which the reconstructed pathways reflect realistic neuronal networks depends, however, on data acquisition and postprocessing factors. Through a unique combination of approaches, we designed and evaluated herein a framework for reliable fiber tracking and mapping of the living mouse brain connectome. One important wiring scheme, connecting gray matter regions and passing fiber-crossing areas, was closely examined: the lemniscal thalamocortical (TC) pathway. We quantitatively validated the TC projections inferred from in vivo tractography with correlative histological axonal tracing in the same wild-type and *reeler* mutant mice. We demonstrated noninvasively that changes in patterning of the cortical sheet, such as highly disorganized cortical lamination in *reeler*, led to spectacular compensatory remodeling of the TC pathway.

fiber tracking validation | brain developmental plasticity

Mapping the brain's neural architecture and its connectivity fingerprints is essential in experimental neuroscience and neurology because connectivity patterns constrain or even define functional neuronal networks (1). Methods for tracing connections in the animal brain have a long history and evolved from silver impregnation (2) of degenerating fibers to the ex vivo visualization of axonally transported tracers injected in different brain nuclei (3), and finally to high-resolution technologies using viral and genetic tracers (4). Exploiting the active transport mechanisms along the axons, the histological tract-tracing methods are of extreme value in addressing neuroanatomical questions in experimental animals, especially when associated with electrophysiological and behavioral observations (5). One challenging and intensively investigated issue is the dynamic interplay between the formation of cortical connectivity and cortical patterning (6). Because of the regional and laminar specificity of axonal targeting, the thalamocortical projection (TCP) system is a primary research focus (7–9); it offers the possibility of examining the way in which cortical patterning and thalamocortical (TC) wiring shape and constrain each other. Axonal tracer studies have produced a large body of evidence concerning TC architecture in experimental animals, suggesting that changes in patterning of the cortical sheet might result in alterations of TC connectivity (10–12). However, axonal tract-tracing is not suitable for monitoring plastic connectivity changes over time in the same individual. Histological visualization of the transported substance is highly invasive and requires the sacrifice of the animal; it allows the identification of only a limited number of pathways terminating in, or originating from, the injection site in a single animal.

One of the most exciting recent developments in neuroimaging, which possibly stands as a noninvasive alternative to histological tracing methods and extends its applicability to human studies, is diffusion tensor (DT)-MRI and consecutive fiber tractography (FT) (13–15). Probing the tissue microstructure by means of spatial encoding of water molecule movements, DT-MRI and FT currently represent the only methodology capable of inferring the ensemble of anatomical connections in the living animal or human brain (16, 17). Several data acquisition methods and an array of tractography algorithms have emerged in the past few years, all of them with the aim of accurately and reproducibly reconstructing specific neural projections. Broadly classified (16) in probabilistic (18, 19), deterministic (20), and the latest global optimization algorithms (21–23), these tractography approaches exploit the assumption that the water molecules' movement in the tissue will be hindered to a higher extent across than along the axons. The directions of greatest diffusion in each voxel will be then used as estimates for fiber orientation. Despite the unique potential of DT-MRI and FT for noninvasive longitudinal investigations in human and animal brains, one of their limitations compared with traditional histological tracing in animals is the spatial scale of the obtained information. Many cellular structures or fiber pathways of biological interest are small in comparison with the scale of the imaging voxel. Increased signal-to-noise ratio (SNR) and further improvement of the spatial resolution could, however, be achieved with high (24, 25) and ultrahigh-field scanners (26), or at the expense of very long acquisition times.

Imaging the mouse brain at 9.4 T and using a postprocessing methodological approach that is generating high-resolution spatial histograms of the diffusion orientations (generally associated with the fibers' orientations), we provide here fine-grained maps inferring the living mouse brain structural connectivity. Exquisite details are revealed by combining a unique global fiber tracking

Significance

Alterations of brain connectional circuits are often associated with developing brain disorders. Pathology, however, can also trigger adaptive brain plasticity and compensatory connectivity changes. This paper provides a verified noninvasive framework for high-resolution mapping of living mouse brain connectional anatomy. We show that pathological changes in the formation of the cortical sheet, such as gross laminar distortions induced by *reelin* gene mutation in mice, lead to spectacular compensatory remodeling of thalamocortical projections. Our findings reveal extensive brain plasticity in the *reeler* mutant mouse, a frequently used model of brain developmental pathology, with great translational value for human brain disorders.

Author contributions: L.-A.H., C.D., J.H., D.v.E., and J.F.S. designed research; L.-A.H., C.D., and J.F.S. performed research; M.R. and S.S. contributed new analytic tools; L.-A.H., C.D., M.R., and J.F.S. analyzed data; and L.-A.H., C.D., and J.F.S. wrote the paper.

The authors declare no conflict of interest.

This article is a PNAS Direct Submission.

[1]L.-A.H. and C.D. contributed equally to this work.

[2]To whom correspondence should be addressed. E-mail: laura.harsan@uniklinik-freiburg.de.

This article contains supporting information online at www.pnas.org/lookup/suppl/doi:10.1073/pnas.1218330110/-/DCSupplemental.

algorithm (21) applied on high angular resolution diffusion imaging (HARDI) data and the above-mentioned methods for generating highly resolved diffusion orientation histograms, referred to here as high-resolution fiber maps (hrFMs) (21, 27). The spatial resolution of the final reconstructed maps is increased several times compared with the scale of the originally acquired data, by incorporating information contained in the whole-brain fiber tracking results. This approach allows verifying and proving the relationship between the fine-grained details captured in the hrFM and the histology results. The outcome is an in vivo mapping of the living mouse brain structural connectome, compared in wild-type and *reeler* mutant animals.

One particular connectivity profile is closely examined and zoomed out noninvasively from the entire ensemble of *reeler* and wild-type brain: the lemniscal TCP, originating in the ventrobasal thalamic nucleus (VB) and terminating in the barrel field of the primary somatosensory cortex (S1BF). The TCP was chosen for two main reasons: (*i*) it is of high functional relevance in rodents (9, 28) as well as humans (29) and (*ii*) it shows a complex 3D trajectory, which is challenging for any fiber tracking algorithm (8). Quantitative measures are also introduced to estimate with probabilistic mapping of connectivity (18, 19), the connection likelihood between these mouse gray matter regions. The accuracy of the connectional information revealed with our imaging approaches is further rigorously assessed. Quantitative validation of the obtained results covering all mouse brain pathways is virtually impossible. Therefore, we provide here a unique proof-of-principle study that validates the TC connectivity profiles generated by using global and probabilistic tractography of the living mouse brain, with correlative histological MicroRuby (MiR) axonal tracing, performed in the same animals. We further investigate noninvasively if changes in patterning of the cortical sheet, especially gross laminar distortions, lead to parallel alterations of TC pathways. As a well-known developmental pathology model with defective formation of layered structures, the *reeler* mutant mouse is a suitable approach (30). In the absence of the *reelin* protein, a key regulator for neuronal migration and cortical development, newborn neurons fail to reach their normal position in the cortical layers (31). The mutation strongly affects the lamination of S1BF (32), giving rise to an anomaly of cortical cytoarchitecture, which should be incompatible with the development of a normal TCP. Therefore, using our validated tools, we directly investigate the hypothesis of brain structural plasticity by massive remodeling of TC axonal trees in the living *reeler* brain.

Results

Global Mouse Brain Fiber Tracking and Generation of hrFM. To explore in vivo the ensemble of living mouse brain fiber pathways as inferred with MR diffusion tractography, we adopted a global fiber tracking approach (21) that processes HARDI data. The algorithm belongs to a class of tractography methods (review in ref. 15) that are building all fibers simultaneously instead of reconstructing tracts one by one, as the classical approaches. More precisely, in global tractography each fiber is formed by small line segments that get bound together; their orientation and number are adjusted simultaneously during optimization; each segment tries to associate with neighboring ones to form longer chains. This behavior is governed by an increasing match to the measured data (21). We previously probed the method on human diffusion data for delineation of well-known human brain connections (21). Here we show a further significant refinement and the first application of our global tracking algorithm for comparative mapping of the living mouse brain structural connectivity in wild-type and *reeler* mutant animals. To get a more refined view of the diffusion orientations generally associated with the orientation of the brain fibers, a further postprocessing step was implemented; this allowed us to produce high-resolution whole-brain histograms of diffusion orientations, i.e., hrFM (Fig. 1; Fig. S1). The increased resolution of the reconstructed maps was achieved by using the track information from the entire voxel neighborhood. The source of contrast in hrFM is based on the density of fibers generated during the global tracking optimization, and passing the image voxel at specific spatial coordinates (*Materials and Methods*). This parameter was used as intravoxel information for increasing the resolution while also incorporating the local fiber directionality information, coded by color. This procedure enabled inferring the overall brain connectivity (Fig. 1; Movie S1). However exquisitely defined, the details captured in the hrFM do not actually feature individual axons; they directly visualize diffusion orientations and, through association, the fibers' orientations. To further qualitatively ex-

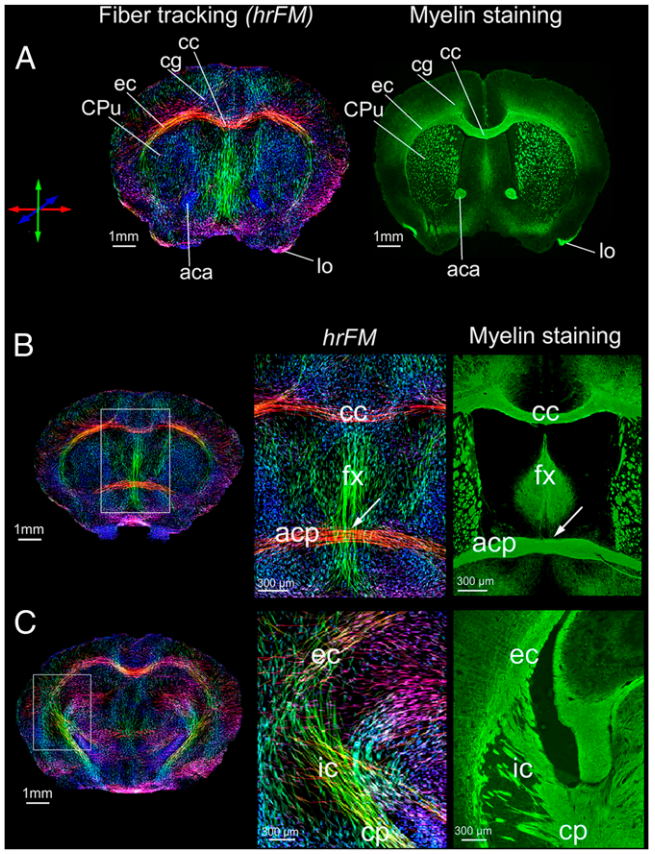

Fig. 1. Living mouse brain connectional anatomy. High-resolution fiber maps generated from the global fiber tracking data and their qualitative comparison with immunofluorescent myelin staining. High qualitative resemblance of hrFM with myeloarchitecture is observed at three different rostrocaudal positions across the mouse brain. (*A*–*C*) Distances from bregma are +0.5, +0.14, and −1.94, respectively. The exemplified hrFM were reconstructed at 15.6 × 15.6 × 50 μm^3 resolution, matching the thickness of the histological tissue slices. The magnified areas in *B* and *C* illustrate the potential of the global tracking algorithm to resolve crossing fiber regions (arrows). The fornix (fx)–anterior commissure (pars posterior; acp) intersection is featured in *B* (magnified) and the complex fiber pathways passing through the internal capsule (ic) from subcortical into the cortical areas (and vice versa) are visible in the magnification of *C*. Various other structures of the mouse brain connectional anatomy could be easily recognized using both in vivo (hrFM) and ex vivo (myelin staining) imaging modalities: (*A*) aca, anterior commissure; anterior part; cg, cc, corpus callosum; cingulum; CPu, caudate putamen; ec, external capsule; lo, lateral olfactory tract. (*B*) acp, anterior commissure, posterior part; fx, fornix. (*C*) cp, cerebral peduncle; ic, internal capsule. The color-coding indicates the local fiber orientation: red, mediolateral; green, dorsoventral; blue, rostrocaudal.

plore the biological basis and the anatomical information content of the obtained tractograms, we compared them with immunohistochemical myelin staining, performed in the same animals. Fig. 1 shows hrFM of the mouse brain, scaled to reach a spatial resolution of 15.6 × 15.6 × 50 μm^3, which represents 10× higher the resolution of the acquired diffusion data (156 × 156 × 500 μm^3) and matching the thickness of the histological sections. Remarkable correspondence between many of the structures visualized in hrFM of the living mouse brain and those identified with myelin staining can easily be recognized (Fig. 1). This feature is visible not only in areas corresponding to gross white-matter anatomy (such as the corpus callosum, anterior commissure, external capsule, internal capsule, and fornix), but also gray matter regions, evidencing, for example, similarities in the striatal texture. Notably, the tracking algorithm also proved its capabilities to resolve fiber-crossing regions (Fig. 1 *B* and *C*, enlarged areas). The possibility to create such highly resolved fiber maps from in vivo diffusion data relied on the capacity of the global tracking approach to generate a sufficiently high number of fibers per voxel to introduce meaningful information. Fig. S1 demonstrates the gain in contrast-to-noise ratio (CNR) and superior delineation of mouse brain fiber tractography with increasing spatial resolution. Fig. S1 *E* and *F* displays sharp delineation of thin tracts emerging from mouse thalamic nuclei, mapped at 11.14 × 11.14 × 35.7 μm^3 resolution. We emphasize that the results were obtained through postprocessing procedures, without the necessary requirement of increasing data acquisition time or at the expense of SNR.

The capability of our approach in terms of in vivo zooming into the fiber architecture to virtually reach a microscopic level was further probed for capturing tractographic features in the presence of brain pathology caused by gene mutation. We therefore used the hrFM to investigate if the general wiring scheme of wild-type mice is preserved in the *reeler* mutant mouse brain, which is known to display severe layering defects (31) (Fig. 2; Movies S1 and S2). Substantial differences were seen between the normal and mutant brain structural connectome. The high-resolution tractograms captured major remodeling features of the sub- and intracortical fiber trajectories reconstructed from the *reeler* diffusion data, (Fig. 2) as well as important modifications within the malformed cerebellum of the *reeler* mutants (Movies S1 and S2). Within the cerebral hemispheres, the most prominent remodeling was noticed inside the TC network. Fig. 2 *C* and *D* captures in hrFM the features of fiber pathway rearrangements in *reeler*. In contrast to the wild-type fiber organization, a striking oblique trajectory linking subcortical areas with superficial layers of the *reeler* cortex is clearly visible within the same plane (Fig. 2*D*; Fig. S2). However, some differences in the cortical and subcortical fiber organization are observed in the hrFM, even between animals from the wild-type group (Fig. S2). Such interindividual variations, potentially including changes in fiber orientations, are difficult to assess quantitatively. We therefore further describe our approach, leading to a quantitative evaluation of diffusion tractography results, while focusing on one specific mouse brain pathway.

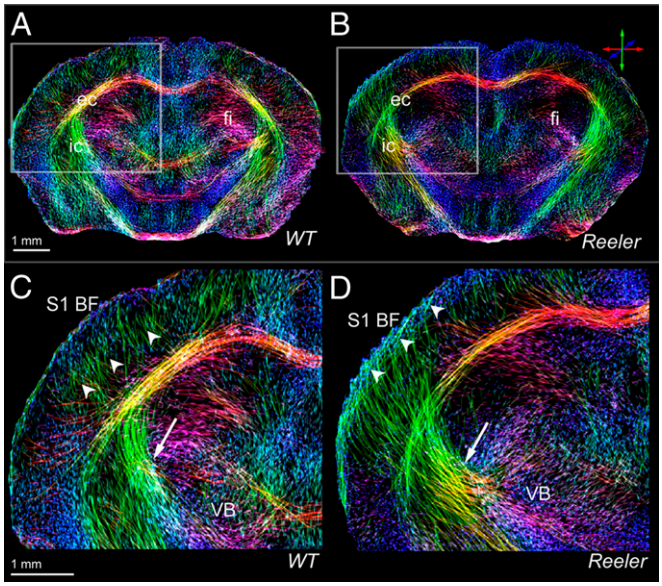

Fig. 2. Comparative high-resolution views of the thalamocortical fiber architecture of the wild-type and *reeler* brain. In vivo hrFM of the wild-type (*A* and *C*) and *reeler* (*B* and *D*) brain captures major features of normal (*C*) vs. remodeled (*D*) subcortical (arrows) and intracortical (arrowheads) fiber trajectories of the somatosensory thalamocortical pathway. The magnified views (*C* and *D*) illustrate the fiber bundles emerging from the VB to target S1BF; they cross the internal capsule (*C* and *D*, arrow) and gather beneath the cortical gray matter before extending intracortically up to presumptive layer IV of the wild-type S1BF (*C*, arrowheads). Note that in comparison with wild type, the *reeler* thalamic fibers (*D*) are defasciculated to form a broader array projecting diagonally (*D*, arrow) into the cortical areas (including S1BF) and forming loops below the pial surface (*D*, arrowheads). The hrFM were reconstructed with 15.6 × 15.6 × 50 μm^3 resolution. The local fiber orientation is color-coded: red, mediolateral; green, dorsoventral; blue, rostrocaudal.

Proof-of-Principle Study: Methodological Validation of in Vivo Thalamocortical Connectivity with MiR Histological Tracing. To verify the in vivo fiber tracking results and to demonstrate the robustness of our approach when crossing gray matter/white matter borders, we further carried out a proof-of principle investigation, focusing on the somatosensory TCP. Specifically, we probed the lemniscal TCP emerging from the VB nucleus of the thalamus targeting the S1BF of the living mouse brain with a complex 3D trajectory. The technical bases are summarized in Fig. 3, and involved a qualitative assessment (Fig. 3 *A–D*) as well as a quantitative (Fig. 3 *E–H*) fiber tracking validation, performed in several steps. First, by means of hrFM, we zoomed into the complex mouse brain wiring scheme reconstructed with global tractography and isolated the VB–S1BF lemniscal pathway (Fig. 3*A*). Second, we introduced a quantitative estimation of the likelihood of connectivity between VB and S1BF, by probabilistic mapping (PM; *Materials and Methods*) of the lemniscal TCP from origin to termination (Fig. 3*B*).

We further probed the accuracy of the connectional information revealed by global fiber tracking and the probabilistic tractograms with correlative MiR histological axonal tracing of the lemniscal TCP (Fig. 3*D*) in the same animals.

Therefore, the same animals examined in vivo with diffusion tractography were further subjected to stereotactically targeted delivery of the MiR axonal tracer into the VB (Fig. 3*D*). This approach resulted in specific labeling of thalamic axons emerging from the injection site and targeting S1BF (and for injections including more ventral parts, as a component of the extra-lemniscal pathway, also S2), subsequently tracing the TCP on serial histological sections. Using coregistering procedures (Fig. S3), the injection sites, clearly visible on the histological sections, were transferred onto the diffusion data. These segmented areas (Fig. S3 *B–E*) were used in the postprocessing steps either as selection regions for the isolation of the TCP reconstructed with the global fiber tracking algorithm (Fig. 3*A*) or as seed areas for the generation of the probabilistic maps of connectivity (Fig. S4). Therefore, a close comparison between in vivo fiber tractography and histological tracing results was performed (Figs. 3–5).

Quantitative validation of the TC connectivity profiles: Probability maps of connectivity vs. axonal density maps. We further introduced a quantitative dimension for the validation of in vivo diffusion-based tractography (Figs. 3 *E–H* and 4). Our approach relied on voxel-wise statistical correlation methods, applied to com-

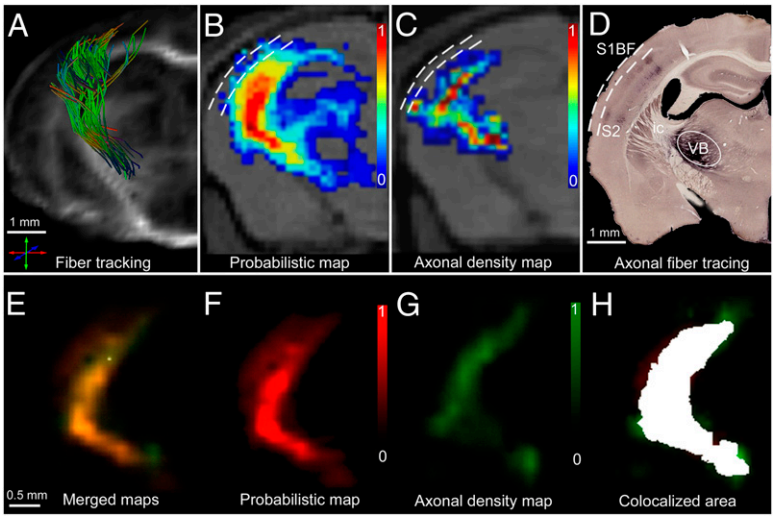

Fig. 3. Quantitative correlation of in vivo fiber tracking (*A* and *B*) and ex vivo histological tracing (*C* and *D*) methods combined with statistical coregistration (*E–H*) in the same animals to study the somatosensory thalamocortical projection. (*A*) A 3D reconstruction of wild-type thalamic fiber bundles emerging from the VB nucleus of the thalamus and superimposed on the corresponding morphological MR images (as in *B* and *C*), originating at the precise location of the MiR axonal tracer injection site (see encircled area in *D*) and projecting into S1BF. The fibers were selected from whole-brain connectivity data generated using our global optimization algorithm. (*B*) PM of connectivity (scaled from 0 to 1) between VB and S1BF. The same PM is represented using the red color channel (scaled from 0 to 1) in *F*. Dashed lines denote the pial surface (external) and the cortical depth corresponding to the layer III/IV border (internal). (*C*) AD maps generated after counting the MiR-labeled axons in histological sections (normalized scale from 0 to 1: 0, no axonal labeling; 1, maximum density of labeled axons obtained in each individual). Compare with *G*, where the same AD map is represented using the green color channel. (*D*) Histological axonal tracing results showing the MiR tracer injection site localized in VB, and the cortical target regions (S1BF and S2). The exemplified histological section was used for the generation of the AD map from *C* and *G*. (*E* and *H*) Statistical coregistration of the PM (*F*) and the AD maps (*G*) of thalamocortical connectivity obtained from the same animal. Merged PM/AD maps (*E*) were produced showing extensive overlap of the pathways generated using the in vivo and ex vivo methodologies. Colocalized area is highlighted in *H* (overlap coefficient of 0.81).

pare PM of TC connectivity (Figs. 3 *B* and *F* and 4*A*) and MiR-labeled axonal density (AD) maps obtained by axonal tracing performed in the same animals (Figs. 3 *C* and *G* and 4*B*). The AD maps were created by counting labeled axonal profiles crossing the plane of the histological section (*Materials and Methods*; Fig. 3 *F–H*; *SI Materials and Methods*, *Generation of the Axonal Density Maps*) using a stereological approach. The spatial location of the counted axons was also registered, relative to anatomical landmarks, such as the brain contour, the ventricular borders, and the major white matter tracts. These landmarks were subsequently used for spatial registration of the AD maps on the diffusion image data, allowing voxel-wise comparison with the corresponding PM.

The quantitative analysis was conducted at two levels. First, an overlap coefficient (r) was calculated to obtain quantitative measures describing the spatial agreement between the TC profiles depicted in vivo in PM and AD maps (Figs. 3*H* and 4*C*). Second, Pearson correlation was carried out, assessing the spatial overlap and the intensity values from the normalized PM and AD maps (Fig. 4*C*; *Materials and Methods*, *MRI–Axonal Tracing Correlations*). One has to consider that the AD maps were generated using 50-μm-thick histological slices, and the probability of connectivity was mapped from diffusion MRI slices of 500-μm thickness. Regardless of this difference in the generation of the two types of maps, we found a high average value for the pathway overlap coefficient (>0.70) in both wild-type and *reeler* animals (Table 1; Figs. 3 *E–H* and 4).

We next investigated the contribution of each type of map to the obtained results by calculating the split Manders coefficients. There might be cases where the AD maps spatially overlap significantly with the PM, but parts of PM do not overlap with the AD topography (false positive pathways when considering the AD maps as the "ground truth"). Reversely, false negative pathways might be identified as parts of the AD maps not overlapping with the corresponding PM. These split Manders coefficients (Manders M_{AD} and M_{PM}) gave quantitative information about how well the maps overlapped. The intersecting regions were highlighted as seen in Fig. 4*C*. Pixel-wise comparison using Pearson coefficients revealed highly significant positive correlation between the AD measures and the PM. The highest positive Pearson correlation was obtained for the sections encompassing the stereotypically organized internal capsule (ic) axons (i.e., Fig. 4, slices 1 and 2 in wild-type and *reeler*). Lower correlation values were calculated in the frontal part of the thalamocortical trajectories (Fig. S5). In these frontal areas, as a general feature, the PMs covered the fields stained by the MiR tracer but extended deeper into striatal regions and along the border of the corpus callosum (Fig. S5, arrows), suggesting some false positive pathways depicted with probabilistic tractography. Fig. 4 exemplifies comparatively the results of the quantitative analysis along the thalamocortical pathway of one wild-type and one *reeler* animal, highlighting the overall significant positive correlation between the PM and AD measures. No significant differences were noticed between the results of PM vs. AD correlations, obtained within each group, emphasizing the reproducibility of the methodological approach.

Moreover, we further asked the question of interindividual variability in the TCP, as generated either with PM or AD approaches. We provide quantitative measures of cross-correlation between the PMs (Fig. S6*A*) of each investigated animal. The same cross-correlation approach was applied for the AD maps (Fig. S6*B*). High positive Pearson correlation coefficients were obtained when comparing the wild-type PMs, indicating a low degree of variability in TCP topology within the wild-type population (Fig. S6*A*, blue). The same trend of significant positive correlation was noticed when cross-comparing the AD maps of the wild-type mice (Fig. S6*B*, blue). A higher degree of interindividual variability was observed when mapping the *reeler* TCP, with both PM (Fig. S6*A*, yellow) and AD approaches (Fig. S6*B*, yellow); this was reflected in the lower (but sig-

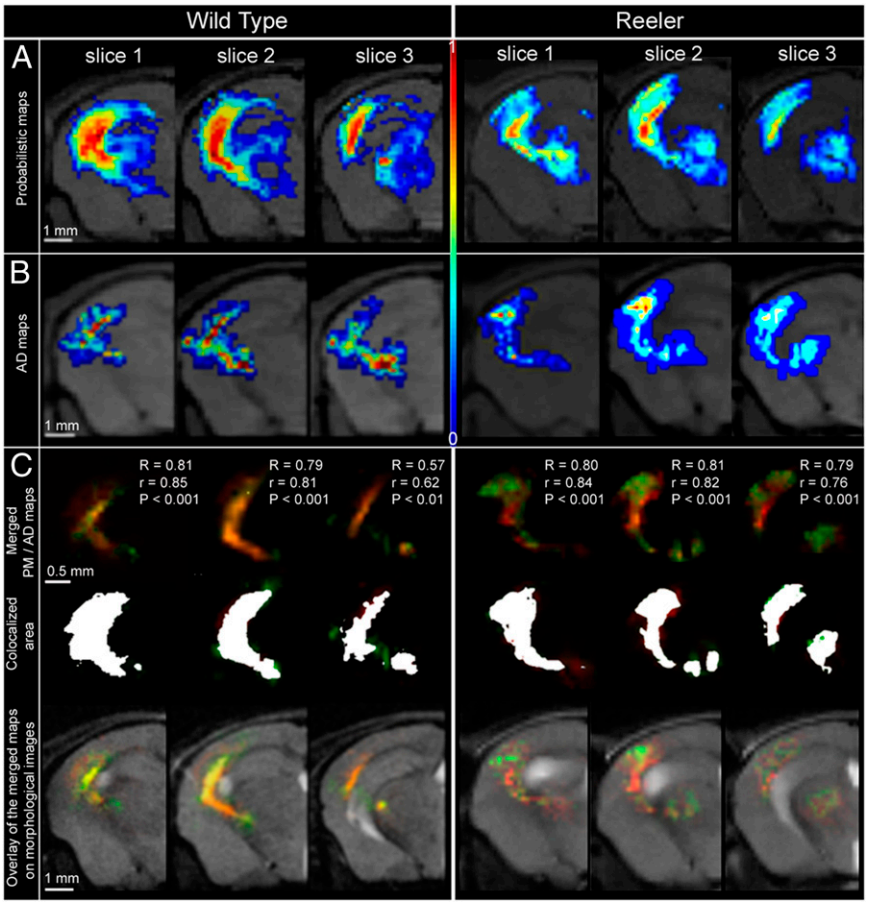

Fig. 4. Quantitative comparison between TCPs derived from in vivo probabilistic mapping (*A*) and ex vivo histological axonal density mapping (*B*) in the same animal demonstrates statistically significant positive correlation throughout all sections (*C*). (*A*) Wild-type (*Left*) and *reeler* (*Right*) TCP representations using in vivo probabilistic mapping. (*B*) Wild-type (*Left*) and *reeler* (*Right*) TCP representations using histological axonal density mapping. (*C*) Statistical coregistration of the PM and AD maps along the TCP (three contiguous slices) in a wild-type (*Left*) and a *reeler* (*Right*) mouse. (*Top*) Merged PM and AD maps and the correlation coefficients. *R*, Pearson coefficient; *r*, overlapping coefficient; $P < 0.001$ and $P < 0.01$ express the significance levels for the comparison of the two mapping results. (*Middle*) Colocalized area for each slice in white. (*Bottom*) Overlay of the merged PM and AD maps on morphological T2-weighted brain images.

nificant) positive correlation when comparing *reeler* PMs (or AD maps).

To quantitatively assess the remodeling of the *reeler* TCP, we additionally performed an interindividual comparison of the PM and AD results, assessing the correlations between animals of different groups (individual wild-type PMs vs. individual *reeler* PMs; and individual wild-type AD maps vs. individual *reeler* AD maps; Fig. S6 *A* and *B*, green). This approach revealed lower wild-type vs. *reeler* correlations in mapping the TCP, probably reflecting the altered topology of this important sensory pathway in the mutant animals.

In vivo origin-to-ending reconstruction of mouse somatosensory TCP reveals extensive remodeling in the* reeler *mutant brain. The projection pattern of wild-type mouse thalamic axons, from the VB to the barrels in cortical layer IV of S1BF (Fig. 5 *B* and *G*), allowed not only testing the in vivo global and probabilistic tractography along the rostrocaudally and mediolaterally contorted subcortical (Fig. 5 *E* and *F*) and cortical pathway sections (Fig. 5 *B* and *G*), but also enabled verification of the terminal fields of this projection (Fig. 5 *A* and *E*, dotted line) against the ground truth provided by the histological tracing (Fig. 5 *B*, dashed lines and *G*). These target fields of thalamic axons are amazingly altered in the *reeler* mutant brains, spanning over nearly the entire thickness of the somatosensory cortex (Fig. 5 *D* and *J*), probably due to the highly disorganized cortical lamination induced by the *reelin* gene mutation. This finding is very much in contrast to earlier studies but in good agreement with recent molecular and functional imaging (32, 33). We therefore focused our investigation on in vivo comparison of the wild-type and *reeler* TCP to get a better understanding of the dynamic interplay between cortical patterning and thalamic axon guidance.

Subcortical section of the somatosensory TCP: Defasciculation of* reeler *axonal projections. Distinctive TC profiles were selectively isolated from wild-type brain tractograms reconstructed with the global fiber tracking algorithm (Fig. 5*E*). Within the subcortical section, tightly clustered fiber bundles emerged from the VB of wild-type mice to form a rostrolateral loop through the ic (Fig. 5*E*). This feature was also obvious in the hrFM (Fig. 2*C*, arrow). After passing the ic, the fibers continue to run tangentially beneath the cortical plate before finally invading the appropriate gray matter regions. The subcortical path, seeded in the MiR tracer injection site, is also very obvious in the PMs of connectivity, emphasizing the high anisotropy along the emerging wild-type thalamic tracts (Fig. 4*A*). A close topographic correspondence was obtained between TC profiles generated in vivo with global tractography and probabilistic mapping as well as axonal tract tracing. The MiR tracer was transported through parallel axonal bundles originating at the injection area (VB), passing through the striatum via the internal capsule to reach the subcortical white matter (Figs. 3*D* and 5*F*).

By contrast, our fiber tracking methods identified a reproducible pattern of defasciculation of the *reeler* thalamic fibers.

Table 1. Quantitative correlation between the PMs derived from diffusion MR data and the AD maps generated from histological axonal tracing in wild-type and *reeler* mice

Mice	Correlation
Wild type	
WT 1	$R = 0.71^{**}$; $r = 0.83$; $M_{AD} = 0.97$; $M_{PM} = 0.85$
WT 2	$R = 0.70^{**}$; $r = 0.78$; $M_{AD} = 0.90$; $M_{PM} = 0.83$
WT 3	$R = 0.73^{***}$; $r = 0.75$; $M_{AD} = 0.97$; $M_{PM} = 0.77$
WT 4	$R = 0.67^{**}$; $r = 0.70$; $M_{AD} = 0.97$; $M_{PM} = 0.72$
WT 5	$R = 0.69^{**}$; $r = 0.80$; $M_{AD} = 0.82$; $M_{PM} = 0.98$
Reeler	
Reeler 1	$R = 0.70^{**}$; $r = 0.81$; $M_{AD} = 0.96$; $M_{PM} = 0.83$
Reeler 2	$R = 0.77^{***}$; $r = 0.89$; $M_{AD} = 0.97$; $M_{PM} = 0.91$
Reeler 3	$R = 0.76^{***}$; $r = 0.83$; $M_{AD} = 0.97$; $M_{PM} = 0.85$
Reeler 4	$R = 0.65^{**}$; $r = 0.71$; $M_{AD} = 0.98$; $M_{PM} = 0.70$
Reeler 5	$R = 0.75^{***}$; $r = 0.84$; $M_{AD} = 0.95$; $M_{PM} = 0.87$

R, Pearson's linear correlation coefficient ranges from −1 to 1 (if 1, perfect positive correlation; if −1, negative correlation, exclusion; if 0, no correlation). The correlation was considered statistically significant when $P < 0.05$ (**very significant correlation for $0.001 < P < 0.001$; ***extremely significant correlation for $P < 0.001$). *r*, Overlap coefficient ranges from 0 to 1: this represents the ratio of the intersecting area to the total nonzero area of both maps. Only nonzero values in each map were included in the analysis. M_{AD}, Manders coefficient representing the fraction of AD overlapping the PM; M_{PM}, Manders coefficient representing the fraction of PM overlapping the AD.

Distorted and poorly organized bundles originated from the VB of the *reeler* thalamus (Figs. 2*D* and 5*H*; Fig. S2); they crossed the ic in a widespread array, ascending directly toward the cortical regions in the same plane, i.e., without extensive looping in the rostrocaudal direction. Furthermore, *reeler* PMs revealed lower indices of connectivity between VB and S1BF compared with the wild-type (Fig. 4 *A*, wild type vs. *reeler*) pathway, suggesting less compact (i.e., more disorganized) thalamocortical bundles passing the *reeler* ic and ascending into the subcortical white matter. This marked feature of defasciculation of the *reeler* subcortical component of the TCP, captured in vivo with diffusion tractography (Fig. 5*H*), was validated by the MiR axonal staining pattern (Fig. 5*I*).

Cortical section of the somatosensory TCP: Remodeling of the* reeler *intracortical terminations. Tracing cortical fibers has been notoriously difficult even when investigating the human brain with diffusion tractography. As fibers approach the gray matter, diffusion anisotropy reduces, and the uncertainty of the principal eigenvector direction increases (34). A global fiber tracking approach allowed for reconstruction of the brain structural connectivity without the use of an anisotropy threshold, and therefore access to the cortical fields with low anisotropy. These areas were also consistently mapped with the probabilistic approach that estimated the probability distribution of the principal diffusion direction and operated remarkably well in the presence of uncertainty. With both methods, clear differences were revealed between the wild-type and the *reeler* cortical connectivity pattern (Fig. 2 *C* vs. *D*, arrowheads; Fig. 5 *A* vs. *C*). When examined with global tractography, the cortical component of the wild-type TCP showed radial projections traversing the cortex and reaching middle layers. Notably, a pattern of clustering of the target points roughly matching layer IV of the S1BF (Fig. 5*E*) was observed. The origin–target specificity of the thalamic axons was evidenced by plotting the starting and ending points for each reconstructed projection (Fig. 5*E*). The PMs, too, indicated terminal fields of the TCP (Fig. 5*A*). High probability connectivity indices were assessed within wild-type S1BF, extending approximately up to neuronal layer IV (i.e., Figs. 3*B*, below lower dashed line and 5*A*, arrow), and this was very much in agreement with the histological tracing pattern (Fig. 5*B*). While penetrating the cortex, the MiR-labeled axons turned pialward to reach their target neurons in layer IV (Fig. 5*B*, arrow). At the bottom of layer IV, the thick thalamocortical axons started to display many collaterals, forming an isotropic cloud that occupies the barrels, and a less-dense upper division reaches the supra-

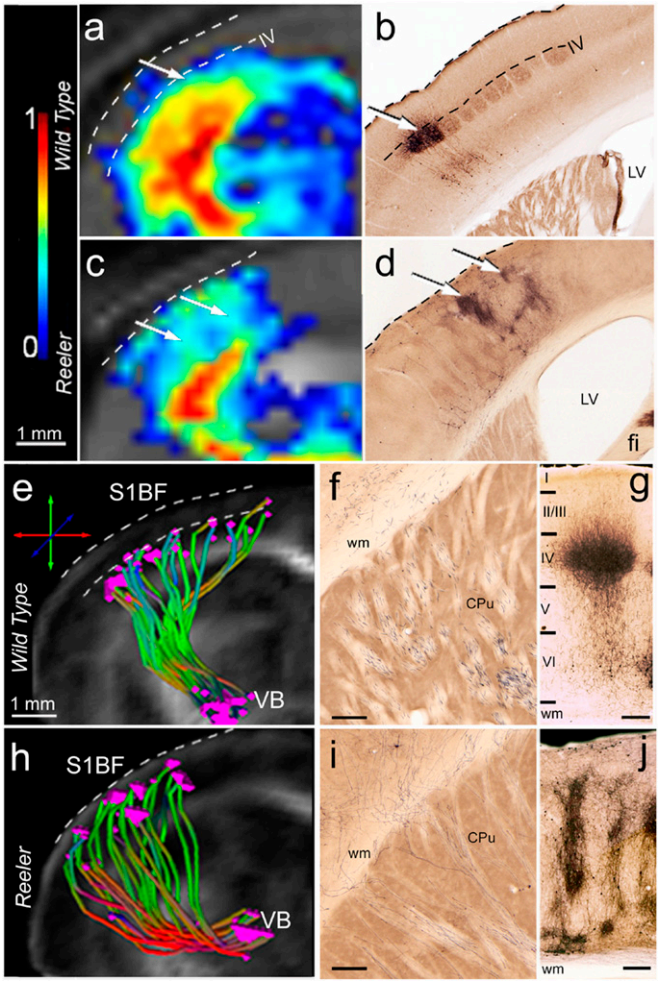

Fig. 5. Intracortical in vivo diffusion-based fiber mapping (*A*, *C*, *E*, and *H*) and histological tracing (*B*, *D*, *F*, *G*, *I*, and *J*) show remodeling of the thalamocortical terminal field in *reeler* mutant compared with wild-type mice. (*A–D*) Probability maps of connectivity (*A* and *C*) depicting fine details of the intracortical portion of the wild-type (*A*) and *reeler* (*C*) TCP, similar to the staining pattern seen in the cortical areas of the same mice after MiR tracer injections (*B* and *D*). Note the distribution of the termination field of the wild-type pathways (*A* and *B*) at the level of cortical layer IV and the extended columnar representation in *reeler* animals (*C* and *D*, arrows). (*E* and *H*) Selective 3D reconstruction of wild-type (*E*) and *reeler* (*H*) thalamic fibers originating in the VB (MiR injection site) and reaching S1BF. The reconstructions reveal subcortical defasciculation and oblique intracortical trajectories of the *reeler* somatosensory thalamocortical projections (*H*) compared with wild-type mice (*E*). The origin and the target points of the identified pathway were plotted for each fiber. The target points of the *reeler* trajectories are distributed across the whole cortical thickness (*H*), contrasting to their clustering at the level of cortical layer IV (upper border depicted by lower dashed line) in wild-type mice (*E*). (*F–J*) Representative subcortical (*F* and *I*) and intracortical (*G* and *J*) MiR tracing of the wild-type (*F* and *G*) and *reeler* (*I* and *J*) TCP. Note the pattern of *reeler* subcortical axons (*I*), reaching the cortex in oblique trajectories, very similar to the pathway identified with global fiber tracking. In S1BF, the main terminal field of the wild-type thalamic projections (*G*) is layer IV. The *reeler* axons are spanning nearly the entire cortical thickness, forming a peculiar columnar pattern (*J*). (Scale bars, 250 μm.)

granular layers (Fig. 5 *B* and *G*). The MiR tracer is known to be transported to some extent retrogradely, too, and therefore the medial lemniscus and some layer VI pyramidal cells (Fig. 5*G*) were labeled, further verifying the correct placement of the injection into the VB. Such a reciprocal connection provides a better comparability with in vivo tractography, because the diffusion tractography pattern cannot distinguish between thalamocortical and corticothalamic connections. Diffusion fiber tracking is only sensitive to the orientation of the fibers but not to their anatomical polarity.

Further examining *reeler* brains, we demonstrated with our in vivo fiber tracking approaches a striking remodeling of the cortical terminal fields. Global tractography and hrFM show the widespread array of *reeler* thalamic axons piercing the cortical plate in an oblique fashion and running diagonally up toward the surface of the cortex (Figs. 2*D* and 5*H*); there they form a loop and descend to different levels in the deeper cortical portions (Fig. 2*D*, arrowheads). Comparative cortical hrFM of wild-type and *reeler* animals are provided in Fig. S7 *A* and *B*, demonstrating that remodeling of intracortical *reeler* connectivity is a general effect observed in all of the investigated animals. Unlike the layer-specific clustering pattern described in wild-type brains, the *reeler* TCP terminals (Fig. 5*H*; Fig. S7*D*) were distributed across the entire depth of S1BF, mirroring the spots where the putative layer IV target neurons erroneously ended their migration. Such effects could not be clearly observed if generating hrFM from tracking results obtained using a local deterministic fiber tracking approach, the fiber assignment by continuous tracking (FACT) algorithm (Fig. S8). The low densities of fibers mapped with FACT do not supply sufficient information for clear differentiation of wild-type vs. *reeler* TC fiber architecture.

We further assumed that the cortical observation described using the global tracking algorithm should be concurrent with divergent modifications of cortical anisotropy indices in wild-type and *reeler* mice. Therefore, we introduced a quantitative dimension to the hrFM results by plotting the fractional anisotropy (FA) values across the whole thickness of the wild-type and *reeler* cortical areas from averaged maps (for each group of mice; Fig. S7 *E* and *F*). These plots showed increased anisotropy at the level of cortical layer IV (where the fiber terminals were clustered) in wild-type animals and a drop of anisotropy indices at the outer edge of this cortical layer. The effect could not be observed in the *reeler* cortex; there, constant FA values were assessed, with a sharp increase in the outmost part of the cortex. The above-described observations were mirrored in the PMs. TC fiber pathway mapped through the *reeler* cortex displayed an oblique columnar appearance and nearly spanned the entire cortical thickness (Figs. 4*A*, *reeler*, and 5*C*), unlike the wild-type pattern with a radial path and a focused termination in layer IV (Fig. 5*A*, arrow). The fine columnar details of thalamocortical connectivity depicted in the PMs (Fig. 5*C*, arrows) were similar to the labeling pattern as seen with the MiR tracer (Fig. 5*D*, arrows). The MiR-labeled axons ascended in irregular profiles through the cortex, approaching the pia, but turning down at the most external cortical surface and unraveling in irregular-formed, columnar clusters (Fig. 5 *D*, arrows and *J*). Taken together, these results demonstrate that the development of the TCPs does not require intact cortical lamination. However, abnormal cortical patterning leads to a parallel alteration of the trajectory and terminal field placement of the thalamocortical axons.

Discussion

Deciphering Connectional Blueprints Across the Living Mouse Brain with Global Tractography. Generating brain-wide maps of human and animal neural connectivity is a major challenge in the basic neuroscience and neuroimaging field (35, 36). Deciphering these connectivity patterns in the mouse is one of the principal aims of the Brain Architecture Project (37). A number of authors (24–27, 38) have elegantly demonstrated the value of MRI diffusion-based tractography in understanding the microstructural mouse brain organization and its intricate connectional anatomy. These ex vivo investigations were performed using ultra- (26, 27) or high-field magnets (24, 25, 38), and revealed brain anatomical details with a resolution of reconstructed fiber density maps reaching 20 μm^3 (27). By using a unique combination of global tractography and fiber-mapping methods, we tailored our hrFM to reach the optical microscopy level, identifying with high definition connectional networks across the whole living mouse brain. The rich anatomical details unveiled biologically meaningful features qualitatively assessed against myelin staining. Using a global tractographic algorithm to process HARDI data provided an important advantage over the common local fiber tracking methods (18, 20)—namely, the ability to reconstruct axonal fibers simultaneously across the whole brain (21). The local algorithms, deterministic (20) or probabilistic (18), construct fibers independently, path by path, and the fibers do not influence each other; their reconstruction is done in small successive steps by following the locally defined distribution of fiber directions. Minor imperfections in the determination of local steps can accumulate and significantly affect the final result (see review in ref. 16). Global tractography infers the orientation information by using a larger field of view, making the estimation of the fiber orientations in ambiguous areas more accurate (21, 22, 39), and better solving the problem of crossing fibers. The algorithm that we used here previously demonstrated its strength by achieving the most accurate results in terms of position, tangent, and curvature of the fibers when quantitatively assessed on a physical phantom, among 10 different tracking approaches (39). An additional benefit of this approach was the exclusion of any boundary conditions prescribing the location of the ends of reconstructed tracts (21). This aspect of the technique was very important because it eliminated a major source of subjectivity and the requirement for any prior knowledge to define seed/target regions for tracking. When combined with hrFM, the method allowed us to evaluate the congruence between tractography results and actual structural connectivity not only for the fiber "highways" but also for the fiber terminations that are generally far below the resolution of current MR hardware.

However, a quantitative validation of diffusion tractography results at a large-scale level, across the whole brain, is particularly difficult to design and perform. The main challenge is to find the most suitable type of histological assessment, which best reflects the fibers' density and spatial orientation. The myelin staining, as used for our qualitative comparison, cannot be considered a ground truth for quantitative validations. Though a majority of axons in the brain are myelinated, the myelin content, as reflected in the histological images, do not have an exact equivalent in diffusion tractography, especially in the gray matter areas. Integrating the results from complementary neuroimaging methods, such as the recently introduced 3D polarized light imaging (36) technique or the Fourier analysis of stained tissue sections (40), holds promise for future comparisons, aiming at the quantitative validation of whole-brain tractography.

Comparatively portrayed for wild-type and *reeler* animals, the large-scale wiring diagrams shown in this study allow a better understanding of the impact of the *reelin* mutation in the formation of the neuronal circuitry. Involved in the guidance of neuronal migration during development, *reelin* has a tremendous implication in the organization of laminated structures (31). In rodents, *reelin* mutation results in the *reeler* phenotype (30, 32), characterized by a major laminar disorganization in the cerebral and cerebellar cortical areas, as well as the hippocampus. *Reelin* mutations in humans have been described and cause lissencephaly with severe mental retardation (41). Recent data (42) have also implied a role for *reelin* in axonal branching and synaptogenesis, further suggesting possible more-subtle modifications of the *reeler* wiring. So far, these important aspects

of the *reeler* phenotype could not be explored in vivo. Therefore, our animal model represents the ultimate test to reveal, in a noninvasive manner, meaningful connectional information using global fiber tractography and high-resolution fiber mapping. Despite a preservation of the general connectional pattern in *reeler* animals, we identified less-defined or remodeled wiring schemes in the *reeler* brain, with the most prominent modifications being found along the TC pathway. Our results demonstrate the feasibility of noninvasive investigations for detecting brain plasticity in mouse models, which opens up great possibilities for high-throughput screening of transgenic mice designed to explore the pathophysiological causes of major human brain diseases (38). It was, however, crucial to introduce a quantitative dimension in our analysis and thus validate our qualitative observations, focusing on a major fiber remodeling observed along the *reeler* TCP.

Probabilistic Mapping of the TCP. Probabilistic tractography (18, 19, 43) assigned confidence to the identified TCP pathways. Multiple possible trajectories emerging from VB and S1BF were calculated and the most probable direct pathway linking the two regions of interest was extracted by using a multiplication approach that suppressed false connecting trajectories (19). No prior assumptions regarding the fiber course were required. The PMs reliably depicted the routes taken by thalamic axonal branches to and within the mouse somatosensory cortex, showing connectivity patterns similar to the MiR axonal tracing results. Moreover, we quantitatively demonstrated, using Pearson correlation, a consistent topology of the TCP derived with PM or AD mapping within the group of wild-type mice. In *reeler* mutants, despite the presence of massive pathology, PMs were able to show cortical plasticity features, such as the barrel-like equivalents spanning, in a columnar pattern, over much of the cortical thickness. A certain degree of interindividual variability in the formation of the *reeler* TCP was quantified. Such variations were reflected in both PMs and AD maps. A consistent estimation of the pathway's terminations was also achieved. The correct identification of the termination area of a specific pathway has long been a critical problem in tractography (15, 16). Here we obtained high values of connection probability in the wild-type cortex up to the level of layer IV, matching well the termination points of the MiR-labeled axons. The *reeler* probabilistic pathways extended inside the cortex up to the outer layers, reaching the pial surface, thereby reflecting the disturbed cortical architecture. We also demonstrate a relationship between pathway termination and increased anisotropy indices in layer IV of wild-type brains and outer cortical layers of *reeler* mice.

Validation of in Vivo Probabilistic TCP with Correlative Axonal Tracing: Quantitative correlation of PM and AD Maps. Our unique approach of comparative analysis involved a demanding quantitative estimation of the number of MiR-labeled axons necessary for the generation of AD maps. This is a unique pixel-wise analysis carried out between the PMs of connectivity and the corresponding AD maps generated from the same animal. Despite abundant literature reporting validation of several tractography methods applied in human (22, 44–46) and animal (17, 47–49) brains or nervous tissue samples (50, 51), we provide here a quantitative evaluation of a framework for fiber tracking and mapping of the living mouse brain, both in normal and pathological conditions. Different from any previous approach comparing diffusion tractography data and histological tract tracing (22, 47, 49), our quantitative comparison relied not only on the estimation of pathway congruence (calculation of the overlapping fraction between PM and AD maps) but also tested the correspondence in the intensity values of the two types of maps. The trajectories overlapped extensively (high r values ranging from 0.7 to 0.89 across the examined mice; Table 1) and a very significant positive correlation between intensity signals in each type of maps was verified (Pearson's R; Table 1) without statistically significant interindividual or intergroup (*wt* vs. *reeler*) variations. An important point in our methodological process was the quantitative assessment of the tractography results in terms of false positive or false negative pathways, measuring the contribution of each map to the overlapping fraction, which showed a few isolated false-positive areas in more rostral regions of the brains in both *wt* and *reeler* mice (*SI Quantitative Correlation: Probabilistic vs. Axonal Density Maps*). Our results therefore allowed estimating the potential of the probabilistic tractography for accurate and reliable mapping of living mouse brain connectivity. We showed the strengths and limitations that are likely to be typical of many of the available tractographic approaches (52). The mouse brain TC projections chosen for investigation provided a three-dimensionally complex trajectory, emerging from the thalamic gray matter, passing white matter/grey matter transitions, and sprouting into the cortical gray matter (7). Hence, the validation benchmark established in this paper will have a high degree of translational value for many other similar rodent brain connection pathways, but also across species.

Developmental Plasticity in the *reeler* Thalamocortical Pathway. Probing the *reeler* brain with diffusion tractography represented an ideal approach for answering a fundamental biological question: Is intact cortical lamination necessary to enable correct wiring with specific thalamic nuclei? Our origin-to-termination TCP mapping clearly demonstrated that changes in patterning of the cortical sheet in *reeler* mutants lead to parallel alterations in the pattern of thalamocortical connectivity. Thalamic fibers from VB are developing alternate routes but finally reach the target neurons spread out across the entire thickness of S1BF (32). This finding suggests the existence of highly specific cell-autonomous target selection mechanisms that control synapse formation in this strongly topographic pathway, and is not compatible with a singular concept based on gradients of attractive and repulsive molecules (7, 53). These results further support our notion that the *reeler* cortex is not simply inverted, and question findings of a concomitantly inverted thalamocortical projection (33, 54). Moreover, probabilistic mapping of the TC projections in subcortical and cortical areas and the MiR axonal tracing revealed a striking feature of the *reeler* cortex: the formation of a unique columnar-like termination pattern of the TCP. This columnar blueprint suggests that although the laminar organization is lost, there is concomitant remodeling of the wild-type barrel equivalents and their afferent thalamic axons to find their target cells within the cortical fields. Although much different in their arborization pattern, the *reeler* TCPs preserve their functional properties, as we previously demonstrated (32). Behavioral stimulation of defined whiskers led to corresponding activation of their columnar modules. We therefore suggest the existence of an active structural and functional plasticity mechanism in the formation and remodeling of the *reeler* TC pathways that needs further study to be disclosed.

Materials and Methods

Animals. Nine adult wild-type female mice and 11 *reeler* mutant female mice (strain B6C3Fe; 7 mo old) were used for whole-brain HARDI, carried out under isoflurane [3% for induction and ~1.5% (vol/vol) for maintenance] mixed with oxygen (1 L/min) anesthesia. The same mice were subsequently used for the histological tracing experiments as described below. The animals were bred and maintained at the University of Freiburg animal facilities, and the breeding and experiments were performed with the approval of the Animal Ethics Committee of the University of Freiburg. For the MRI experiments, the animals were placed in a stereotaxic device to immobilize the head. A heating pad maintained the body temperature at 37 °C. The anesthetic's concentration was permanently adjusted in accordance with changes in respiratory rate, which was constantly monitored.

MRI Data Acquisition and Postprocessing. *Acquisition.* MRI was performed with a 9.4-T small-bore animal scanner, a transmit/receive 1H mouse quadrature birdcage resonator (35 mm inner diameter), and the ParaVision 5 software interface (Biospec 94/20; Bruker). The magnetic field homogeneity was optimized by performing a localized shimming procedure on a volume of interest ($4.8 \times 5.3 \times 9$ mm^3) placed inside the mouse brain. This step of the imaging protocol was designed to correct the distortions and signal intensity dropout caused by local susceptibility differences between adjacent structures (particularly observed in border regions). For this optimization, we used the press waterline spectroscopy protocol as well as FastMap procedures provided with the Bruker ParaVision 5 system.

Diffusion MRI data were acquired using a four-shot DT-echo planar imaging sequence [repetition time, 7,750 ms; echo time, 20 ms; time (Δ) between the application of diffusion gradient pulses, 10 ms; diffusion gradient duration (δ), 4 ms; gradient amplitude (G), 46.52 mT/m]. The acquisition protocol included the use of 30 gradient diffusion directions (Jones 30 encoding scheme), as previously described by us (43), using a b-factor of 1,000 s/mm^2. The high angular resolution of the diffusion weighting directions improves the signal-to-noise ratio and reduces the directional bias during fiber tracking, extracting local information at fiber-crossing regions. The in-plane image resolution was 156×156 μm at a field of view of 20×20 mm and an acquisition matrix of 128×92. Partial Fourier with an acceleration factor of 1.35 and 31 overscan lines were used. Morphological T1- and T2-weighted images of the whole mouse brain were also acquired with RARE T2- and T1-weighted sequences ($78 \times 78 \times 500$ μm^3 resolution). These investigations resulted in a total imaging time of ~2 h for each animal (99 min for HARDI acquisition; 21 min for T1- and T2-weighted images).

MRI data postprocessing. Diffusion data postprocessing was performed using the FiberTool package (www.uniklinik-freiburg.de/mr/live/arbeitsgruppen/diffusion/fibertools_en.html) developed in-house. Two fiber tracking approaches were used comparatively to define the mouse brain neuronal networks. The first approach used a global fiber tracking algorithm that processes HARDI data, proposing globally optimized solutions for the whole-brain fiber pathways to be obtained (21). The second approach was based on a probabilistic algorithm (19) capable of estimating the probability distribution of the principal diffusion direction in each voxel and generating probability maps of connectivity that define the TCP.

Global fiber tracking. The method used in our study (detailed in *SI Materials and Methods, Global Fiber Tracking*) is reconstructing all fiber bundles simultaneously, for the whole brain, without the requirement of defining seed or target regions. The principles of the approach were published in a previous study (21). The reconstructed fibers are built with small line segments (particles) described by a spatial position and orientation; their orientation and number are adjusted simultaneously, and the connections between segments are formed based on a probabilistic hopping that retains features of the known probabilistic tracking algorithms. The reconstructions contain several hundred of these segments per voxel; their behavior is governed by certain parameters, classified in two categories: (*i*) cylinder parameters–geometrical parameters of the fiber model and (*ii*) parameters concerning the iteration process. For the global reconstruction of the mouse brain fibers, the optimization was based on previous application to the human brain diffusion data (21) and on preliminary visual assessment of the tracking results. Histological myelin staining of mouse brain tissue sections was used for comparison during this empirical tuning.

Generation of hrFM. To generate the hrFM, the number of tracts in each element of a grid (defining the desired resolution of the maps) was calculated from whole-mouse brain fibers in a manner very similar to previously published methodology (21, 27). The grid size used for comparatively mapping the global wild-type and *reeler* brain connectivity was tailored to match the thickness of the tissue sections (50 μm) used for revealing the MiR axonal tract-tracing (see below). Therefore, the final map had a resolution 10× higher than the actual resolution of the acquired diffusion data (Figs. 1 and 2; Fig. S1). The method used the continuity information contained in the fibers reconstructed during the global tracking procedure, to introduce subvoxel information based on supporting information from neighboring voxels. After the generation of sufficient number of fibers passing a voxel at different spatial locations, their density was used as intravoxel information to construct the hrFM. The directionality of the fibers was incorporated into the hrFM by assigning red/green/blue color to different spatial directions: red: mediolateral, green: dorsoventral; and blue: rostrocaudal orientation. Therefore, our hrFM represent highly resolved spatial histograms of diffusion orientations, where the orientations are fitted to the diffusion data. In the visualization of the data, a single reconstructed fiber should not be associated with the representation of a single axon but rather with a fiber tract gathering an unknown multiple of axons.

Reconstruction of the thalamocortical projections. For specific identification of the thalamocortical pathway from the ensemble of mouse brain fiber tracts reconstructed with the global tracking algorithm, we selected exclusively the fibers crossing both the MiR tracer injection site (VB) and the target region (S1BF; Fig. S3). Defined origin-to-termination tractography of the thalamocortical projections was performed by additionally mapping the starting and the ending points of the selected fibers (Fig. 5 *E* and *H*). For more information, see *SI Materials and Methods, Reconstruction of the Thalamocortical Projections*, and Fig. S3.

Generation of probabilistic maps of connectivity. A fiber tracking probabilistic approach (19) capable of determining the most probable pathway connecting two seed regions was used (19, 43). The procedure was applied for depicting the connectivity pattern between two seed points, the VB (MiR tracer injection site) and the S1BF (target region) in wild-type and *reeler* animals. The method required two processing steps (19, 43) exemplified in Fig. S4 and detailed in *SI Materials and Methods, Generation of Probabilistic Maps of Connectivity*. The final PM represents a voxel-wise estimation of the probability indices that a voxel is part of the VB–S1BF connecting fiber bundle. The minimum and maximum of all of the maps were scaled between 0 and 1. For quantitative comparison, the PMs of connectivity were further coregistered and quantitatively correlated with the AD maps generated from the MiR axonal tracing experiments (see below).

MiR Tracer Injections, Tissue Processing, Visualization, and Reconstruction of MiR-Labeled AD Maps. Several days after the mouse brain diffusion data acquisition, the same animals were subjected to axonal tracing experiments. Precise iontophoretic delivery (55) of MiR (Invitrogen) axonal tracer into the VB was performed (*SI Materials and Methods, MiR Tracer Injections*). This nucleus, similar to other subcortical structures and in contrast with the cortical areas, is not ostensibly influenced by the *reelin* mutation (32). Due to the small size of the mouse VB, the number of successful injections was smaller than the MRI scans. Nevertheless, five wild-type and five *reeler* injections were completely restricted to the VB, resulting in accurate axonal tracings suitable for evaluation. The animals were further kept alive for 48 h to enable the transport of the tracer over the whole length of the thalamic axons, followed by brain harvesting and histological detection (56) of MiR-labeled axons, revealing the TCP (*SI Materials and Methods, Histological Detection of the MiR-Labeled Axons*).

Generation of the AD maps. With the aim of performing a quantitative correlation between the MRI tractography results featuring the TCP and the classical anatomical tracing, density maps of the MiR-labeled axons were created. Each 10th 50-μm-thick histological section was evaluated using an Eclipse 80i microscope (Nikon) and Neurolucida 3D reconstruction software (MBF Biosciences) by counting the labeled axonal profiles crossing the probe plane (57, 58). At the same time, the 3D position of the axonal profiles was also registered, and axonal density maps were further generated (Figs. 3 *C* and *G* and 4*B*) and saved as ASCII files. For further information, see *SI Materials and Methods, Generation of the Axonal Density Maps*.

MRI–Axonal Tracing Correlations. The ASCII files (obtained with Neurolucida software) containing the MiR tracing-derived information about the labeled axons' density were processed using MatLab scripts and transformed in a map format similar to the probabilistic maps (Fig. 4*B*). An average of the axonal density in each 156×156 μm^2 of brain tissue (50-μm section thickness) was calculated and intensity values were assigned, ranging from 0 to 1 (0: no labeled axons; 1: highest axonal density/voxel obtained from all of the sections analyzed per animal). Together with the axonal density information, the generated maps also contained the spatial landmarks (the brain contour, the white matter, and the ventricular borders). These landmarks were further used to register the AD maps over the corresponding non–diffusion-weighted A0 images (using the same ImageJ plug-ins previously used for coregistering the MRI and histological sections) (59), and therefore allowing the quantitative pixel-wise comparison with the PMs of connectivity generated from the same animal. Pearson's linear (*R* coefficient) correlation algorithms were applied for each pair of AD–PM (ranging from −1 to 1: if 1, perfect positive correlation; if −1, negative correlation, exclusion; if 0, random localization). The statistical analysis was performed pixel by pixel, and the *P* values were calculated to evaluate the significance of the correlation. The overlap coefficient (*r*: ranging from 0, no overlap, to 1, perfect overlap) and the Manders split coefficients (60) (if 1, perfect colocalization; if 0, no colocalization; M_{AD}, fraction of AD overlapping PM; M_{PM}, fraction of PM overlapping AD) were obtained.

Quantitative Evaluation of Interindividual Variations in the TCP Topology. Individual PMs from each animal were spatially normalized (using ImageJ plug-ins) over the PM of wild-type mouse 1 (*WT1*) considered as template. Statistical cross-correlation analysis was performed (using Pearson's correlation algorithm) to check for interindividual correlations of the probability

maps derived from in vivo diffusion MR data. The same approach was applied for assessing interindividual correlations of the axonal density maps derived from histological axonal tracing.

ACKNOWLEDGMENTS. We thank Dr. Matthew Budde for kindly providing the ImageJ plug-in used for registration of histological and MRI images and Dr. Valerij Kiselev for very helpful discussions regarding the global tracking algorithm. This work was supported by Deutsche Forschungsgemeinschaft Grant SFB780 TP C1, the BrainLinks - BrainTools Freiburg Cluster of Excellence (MouseNet, P31), and the Center of Molecular Physiology of the Brain, Göttingen (B1). L.-A.H. was supported by a Humboldt Foundation Postdoctoral Grant. Publication costs were supported by the Neurex network (www.neurex.org).

1. Johansen-Berg H, et al. (2005) Functional-anatomical validation and individual variation of diffusion tractography-based segmentation of the human thalamus. *Cereb Cortex* 15(1):31–39.
2. Nauta WJ (1993) Some early travails of tracing axonal pathways in the brain. *J Neurosci* 13(4):1337–1345.
3. Vercelli A, Repici M, Garbossa D, Grimaldi A (2000) Recent techniques for tracing pathways in the central nervous system of developing and adult mammals. *Brain Res Bull* 51(1):11–28.
4. Lichtman JW, Livet J, Sanes JR (2008) A technicolour approach to the connectome. *Nat Rev* 9(6):417–422.
5. Bock DD, et al. (2011) Network anatomy and in vivo physiology of visual cortical neurons. *Nature* 471(7337):177–182.
6. O'Leary DD, Chou SJ, Sahara S (2007) Area patterning of the mammalian cortex. *Neuron* 56(2):252–269.
7. Lopez-Bendito G, Molnar Z (2003) Thalamocortical development: How are we going to get there? *Nat Rev* 4(4):276–289.
8. Behrens TE, et al. (2003) Non-invasive mapping of connections between human thalamus and cortex using diffusion imaging. *Nat Neurosci* 6(7):750–757.
9. Yu X, et al. (2012) Thalamocortical inputs show post-critical-period plasticity. *Neuron* 74(4):731–742.
10. Garel S, Yun K, Grosschedl R, Rubenstein JL (2002) The early topography of thalamocortical projections is shifted in Ebf1 and Dlx1/2 mutant mice. *Development* 129(24):5621–5634.
11. Mallamaci A, Muzio L, Chan CH, Parnavelas J, Boncinelli E (2000) Area identity shifts in the early cerebral cortex of Emx2$^{-/-}$ mutant mice. *Nat Neurosci* 3(7):679–686.
12. Bishop KM, Goudreau G, O'Leary DD (2000) Regulation of area identity in the mammalian neocortex by Emx2 and Pax6. *Science* 288(5464):344–349.
13. Le Bihan D (2003) Looking into the functional architecture of the brain with diffusion MRI. *Nat Rev* 4(6):469–480.
14. Mori S, Zhang J (2006) Principles of diffusion tensor imaging and its applications to basic neuroscience research. *Neuron* 51(5):527–539.
15. Jbabdi S, Johansen-Berg H (2011) Tractography: Where do we go from here? *Brain Connect* 1(3):169–183.
16. Jones DK (2008) Studying connections in the living human brain with diffusion MRI. *Cortex* 44(8):936–952.
17. Parker GJ, et al. (2002) Initial demonstration of in vivo tracing of axonal projections in the macaque brain and comparison with the human brain using diffusion tensor imaging and fast marching tractography. *Neuroimage* 15(4):797–809.
18. Parker GJ, Haroon HA, Wheeler-Kingshott CA (2003) A framework for a streamline-based probabilistic index of connectivity (PICo) using a structural interpretation of MRI diffusion measurements. *J Magn Reson Imaging* 18(2):242–254.
19. Kreher BW, et al. (2008) Connecting and merging fibres: Pathway extraction by combining probability maps. *Neuroimage* 43(1):81–89.
20. Mori S, Crain BJ, Chacko VP, van Zijl PC (1999) Three-dimensional tracking of axonal projections in the brain by magnetic resonance imaging. *Ann Neurol* 45(2):265–269.
21. Reisert M, et al. (2011) Global fiber reconstruction becomes practical. *Neuroimage* 54(2):955–962.
22. Li L, et al. (2012) Quantitative assessment of a framework for creating anatomical brain networks via global tractography. *Neuroimage* 61(4):1017–1030.
23. Jbabdi S, Woolrich MW, Andersson JL, Behrens TE (2007) A Bayesian framework for global tractography. *Neuroimage* 37(1):116–129.
24. Jiang Y, Johnson GA (2010) Microscopic diffusion tensor imaging of the mouse brain. *Neuroimage* 50(2):465–471.
25. Aggarwal M, Mori S, Shimogori T, Blackshaw S, Zhang J (2010) Three-dimensional diffusion tensor microimaging for anatomical characterization of the mouse brain. *Magn Reson Med* 64(1):249–261.
26. Moldrich RX, et al. (2010) Comparative mouse brain tractography of diffusion magnetic resonance imaging. *Neuroimage* 51(3):1027–1036.
27. Calamante F, et al. (2012) Super-resolution track-density imaging studies of mouse brain: comparison to histology. *Neuroimage* 59(1):286–296.
28. Kim YB, Kalthoff D, Po C, Wiedermann D, Hoehn M (2012) Connectivity of thalamo-cortical pathway in rat brain: Combined diffusion spectrum imaging and functional MRI at 11.7 T. *NMR Biomed* 25(7):943–952.
29. Diamond ME, et al. (2008) 'Where' and 'what' in the whisker sensorimotor system. *Nat Rev* 9(8):601–612.
30. D'Arcangelo G (2005) The *reeler* mouse: Anatomy of a mutant. *Int Rev Neurobiol* 71: 383–417.
31. Tissir F, Goffinet AM (2003) *Reelin* and brain development. *Nat Rev Neurosci* 4(6): 496–505.
32. Wagener RJ, Dávid C, Zhao S, Haas CA, Staiger JF (2010) The somatosensory cortex of *reeler* mutant mice shows absent layering but intact formation and behavioral activation of columnar somatotopic maps. *J Neurosci* 30(46):15700–15709.
33. Caviness VS, Jr., Frost DO (1983) Thalamocortical projections in the *reeler* mutant mouse. *J Comp Neurol* 219(2):182–202.
34. Jones DK (2003) Determining and visualizing uncertainty in estimates of fiber orientation from diffusion tensor MRI. *Magn Reson Med* 49(1):7–12.
35. Leergaard TB, Hilgetag CC, Sporns O (2012) Mapping the connectome: Multi-level analysis of brain connectivity. *Front Neuroinform* 6:14.
36. Axer M, et al. (2011) A novel approach to the human connectome: Ultra-high resolution mapping of fiber tracts in the brain. *Neuroimage* 54(2):1091–1101.
37. Bohland JW, et al. (2009) A proposal for a coordinated effort for the determination of brainwide neuroanatomical connectivity in model organisms at a mesoscopic scale. *PLOS Comput Biol* 5(3):e1000334.
38. Ren T, Zhang J, Plachez C, Mori S, Richards LJ (2007) Diffusion tensor magnetic resonance imaging and tract-tracing analysis of Probst bundle structure in Netrin1- and DCC-deficient mice. *J Neurosci* 27(39):10345–10349.
39. Fillard P, et al. (2011) Quantitative evaluation of 10 tractography algorithms on a realistic diffusion MR phantom. *Neuroimage* 56(1):220–234.
40. Budde MD, Janes L, Gold E, Turtzo LC, Frank JA (2011) The contribution of gliosis to diffusion tensor anisotropy and tractography following traumatic brain injury: Validation in the rat using Fourier analysis of stained tissue sections. *Brain* 134(Pt 8): 2248–2260.
41. Mochida GH (2009) Genetics and biology of microcephaly and lissencephaly. *Semin Pediatr Neurol* 16(3):120–126.
42. Leemhuis J, et al. (2010) Reelin signals through apolipoprotein E receptor 2 and Cdc42 to increase growth cone motility and filopodia formation. *J Neurosci* 30(44):14759–14772.
43. Harsan LA, et al. (2010) In vivo diffusion tensor magnetic resonance imaging and fiber tracking of the mouse brain. *NMR Biomed* 23(7):884–896.
44. Clatworthy PL, et al. (2010) Probabilistic tractography of the optic radiations—an automated method and anatomical validation. *Neuroimage* 49(3):2001–2012.
45. Lawes IN, et al. (2008) Atlas-based segmentation of white matter tracts of the human brain using diffusion tensor tractography and comparison with classical dissection. *Neuroimage* 39(1):62–79.
46. Hansen B, et al. (2011) Diffusion tensor microscopy in human nervous tissue with quantitative correlation based on direct histological comparison. *Neuroimage* 57(4): 1458–1465.
47. Dauguet J, et al. (2007) Comparison of fiber tracts derived from in-vivo DTI tractography with 3D histological neural tract tracer reconstruction on a macaque brain. *Neuroimage* 37(2):530–538.
48. Dauguet J, et al. (2007) Three-dimensional reconstruction of stained histological slices and 3D non-linear registration with in-vivo MRI for whole baboon brain. *J Neurosci Methods* 164(1):191–204.
49. Dyrby TB, et al. (2007) Validation of in vitro probabilistic tractography. *Neuroimage* 37(4):1267–1277.
50. Leergaard TB, et al. (2010) Quantitative histological validation of diffusion MRI fiber orientation distributions in the rat brain. *PLoS ONE* 5(1):e8595.
51. Flint JJ, et al. (2010) Cellular-level diffusion tensor microscopy and fiber tracking in mammalian nervous tissue with direct histological correlation. *Neuroimage* 52(2): 556–561.
52. Bastiani M, Shah NJ, Goebel R, Roebroeck A (2012) Human cortical connectome reconstruction from diffusion weighted MRI: The effect of tractography algorithm. *Neuroimage* 62(3):1732–1749.
53. Maruyama T, Matsuura M, Suzuki K, Yamamoto N (2008) Cooperative activity of multiple upper layer proteins for thalamocortical axon growth. *Dev Neurobiol* 68(3): 317–331.
54. Higashi S, Hioki K, Kurotani T, Kasim N, Molnár Z (2005) Functional thalamocortical synapse reorganization from subplate to layer IV during postnatal development in the reeler-like mutant rat (shaking rat Kawasaki). *J Neurosci* 25(6):1395–1406.
55. Paxinos G, Franklin K (2001) *The Mouse Brain in Stereotaxic Coordinates* (Academic, London).
56. Wong-Riley MT, Welt C (1980) Histochemical changes in cytochrome oxidase of cortical barrels after vibrissal removal in neonatal and adult mice. *Proc Natl Acad Sci USA* 77(4):2333–2337.
57. Calhoun ME, Mouton PR (2001) Length measurement: New developments in neurostereology and 3D imagery. *J Chem Neuroanat* 21(3):257–265.
58. Schmitz C, Hof PR (2005) Design-based stereology in neuroscience. *Neuroscience* 130(4):813–831.
59. Budde MD, Xie M, Cross AH, Song SK (2009) Axial diffusivity is the primary correlate of axonal injury in the experimental autoimmune encephalomyelitis spinal cord: A quantitative pixelwise analysis. *J Neurosci* 29(9):2805–2813.
60. Manders EM, Verbeek FJ, Aten JA (1993) Measurement of co-localization of object in dual-colour confocal images. *J Microsc* 169:375–382.